Describing Function Method Based Power Oscillation Analysis of *LCL*-Filtered Single-Stage PV Generators Connected to Weak Grid

Yanghong Xia, *Student Member, IEEE*, Miao Yu, *Member, IEEE*, Xiaoming Wang, and Wei Wei

***Abstract*—For the *LCL*-Filtered single-stage photovoltaic (PV) generators, the low-frequency power oscillation (<50 Hz) occurs frequently when they are connected to the weak grid, whose oscillation mechanism has been a hot topic recently. However, the existing stability analysis methods rarely take the complete model of the PV generators into consideration, thus the accuracy and completeness of the corresponding conclusions are influenced. In this paper, a novel stability analysis method is proposed to obtain the more accurate and complete results for the *LCL*-Filtered single-stage PV generators. First, the complete model of the PV generators is established including the perturbation and observation (P&O) based PV power loop and dc voltage loop, which are rarely considered by the existing stability analysis methods. Especially, the P&O based PV power loop is nonlinear and discontinuous, and the conventional small-signal modeling is inapplicable. Hence, its influence is completely ignored in the existing stability analysis methods. Second, considering the nonlinear discontinuous link, the describing function method is adopted to analyze the whole system stability based on the established complete model. In this way, the accuracy and completeness of the stability analysis are enhanced. Furthermore, for the critically stable state, both the oscillation amplitude and frequency can be calculated accurately. At the same time, different influence factors are analyzed quantitatively including the operation points, grid strength, and the interaction of multiple control loops. It is first revealed that the grid impedance has different influence on the system high-frequency and low-frequency stability. Also, the proposed analysis method and the conventional method are compared, which presents the advantages of the proposed analysis method. Finally, all the theoretical analyses are verified by the real-time hardware-in-loop tests.**

***Index Terms*—Describing function (DF) method, *LCL* filter, low-frequency power oscillation, single-stage PV generators, stability analysis.**

Manuscript received July 11, 2018; revised September 30, 2018; accepted December 12, 2018. Date of publication December 17, 2018; date of current version June 10, 2019. This work was supported by the National Key R&D Program of China under Grant 2017YFB0902000 and Science and Technology Project of State Grid under Grant SGXJ0000KXJS1700841. Recommended for publication by Associate Editor J. A. Oliver. *(Corresponding author: Miao Yu.)*

The authors are with the College of Electrical Engineering, Zhejiang University, Hangzhou 310027, China (e-mail:

grid current regulation without active damping, the stability and robustness of grid-connected *LCL*-Filtered converters against the grid impedance variation is studied in the discrete domain (z-domain) [11]. The relationship between system stability and the ratio of resonance frequency over sampling frequency is revealed and the system control gain limit is calculated. At the same time, it is shown that the grid-voltage feedforward regulator would significantly alter the system stability in the weak grid. In [12], it was presented that for the typical grid current feedback active damping, a contradiction between the high bandwidth and the high robustness exists. Therefore, the grid current feedback active damping cannot work well for wide grid impedance variation. Then, based on the impedance analysis, an impedance-phase shaping compensator is proposed to assure the high robustness with a proper bandwidth. In [13], the influence of control delay on the grid current feedback active damping is carefully analyzed. It is found that the control delay can greatly change the critical frequency of the system where the equivalent virtual resistance of the active damping is positive or not, thus the system stability is influenced. Then, a lead-grid-current-feedback-resonance-suppression method is proposed to reduce the control delay.

The above literatures are mainly about the high-frequency instability. However, the low-frequency instability is also easy to occur in the field and has more adverse effects for the interconnecting devices in the power system. Hence, some researchers also paid attention to the possible reasons of the low-frequency instability [14]–[17]. In these literatures, more control loops especially phase-locked loop (PLL) are taken into consideration and the dc side of the PV generator is still viewed as an ideal voltage source. In [14], the impedance-based stability criterion is proposed for the grid-connected inverters when they are connected to the weak grid. Through the impedance analysis, the power oscillation frequency can be approximately predicted. Chen *et al.* [15] build the output impedance model of *LCL*-Filtered single-phase converters considering the control delay and PLL. Then, based on the impedance analysis, an impedance-phase compensation strategy was proposed to increase the phase margin of the grid-connected converter and enhance the adaptability against the variation of the grid impedance. In [16], a power-voltage control strategy instead of the conventional power-current strategy was proposed for the grid-connected *LCL*-Filtered three-phase converters to improve the ability of outputting power. Furthermore, a *d–q* frame based impedance model was established with consideration of PLL to study the influence of the grid strength, which proves the good robustness of this power-voltage control strategy. Zhou *et al.* [17] thought that the current control loop interacts with PLL via the voltage of the point of common coupling when the *LCL*-Filtered converters are attached to weak grid. As a result, PLL dynamic might deteriorate grid current control and even cause system instability. Then, they suggested that through optimizing parameters, the negative effect of PLL on current control can be reduced effectively.

Also, many scholars think that some nonlinear links in the *LCL*-Filtered single-stage PV generators may cause the instability [18]–[22], where the dc side of the PV generator is still viewed as an ideal voltage source and the whole PV generator system is simplified into a voltage-source converter (VSC). Paquette and Divan [18] pointed out that the current limitation used to avoid overloads will result in the synchronous instability between the VSC and the synchronous generator. That is, the frequency of the VSC diverges from the frequency of the synchronous generator, then *dq*-axis voltages of the VSC begin to "wind up" and form persistent oscillation. However, the corresponding unstable mechanism is not well explored. To understand the theory behind this synchronous instability better, the quasistatic transient stability analysis is conducted in [19] and [20]. Through the analysis, the evolution process is clearly presented and the instability can be well explained. However, the proposed stability analysis method is based on the quasistatic model where the dynamics of voltage loop, current loop, *LCL* filters, and so on are completely omitted; hence, the accuracy of the result is influenced and the other possible induction factors are buried. In [21] and [22], the input saturation due to the hard limitation on the duty cycle which belongs to [0, 1] is investigated based on the Lyapunov function. It is found that the input saturation has significant influence on the stability of converters and causes some nonlinear phenomena. But the Lyapunov function cannot provide some more physical insights, so the unstable mechanism is not reflected directly or clearly.

From the above narration, it can be seen that the existing stability analysis methods do not take the complete model of the PV generators into consideration like the dynamics of PV panels, dc voltage loop, and the outmost perturbation and observation (P&O) based PV power control loop. Hence, the accuracy and completeness of the corresponding conclusions are influenced. In particular, the explanation for the low-frequency ($<$50 Hz) oscillation is not so satisfactory. To fill in this gap, this paper adopts the describing function (DF) method to analyze the stability of the *LCL*-Filtered single-stage PV generator with consideration of the complete control loops when it is connected to the weak grid. First, the complete model of the PV generator is established including PLL, dynamics of PV panels, and P&O-based PV power control simultaneously. Being different from the existing stability analysis methods, the nonlinear discontinuous P&O-based PV power control, which cannot be modeled by the conventional small-signal method, is taken into consideration in the proposed analysis method. Hence, its influence, which is completely ignored in the existing stability analysis methods, can be carefully studied. In addition, the high-order *LCL* filter is not simplified and it is considered together with other control loops, which can improve the accuracy of the results effectively. Second, based on the established complete model of the *LCL*-Filtered single-stage PV generator, the DF method is adopted to analyze the system stability. Compared to the commonly used small-signal modeling, which is the time-domain approximation, the DF method is the frequency-domain approximation and the nonlinear discontinuous elements can be taken into consideration in the frequency domain. In this way, the accuracy and completeness of the stability analysis are enhanced. Especially for the critically stable state, both the oscillation amplitude and frequency can be calculated accurately. At the same time, different influ-

TABLE I
COMPARISON WITH EXISTING STABILITY ANALYSIS METHODS

Analysis Methods	Type		Modelling						Effects	
	Small-signal	Large-signal	Nonlinear Link	PV Power & Dc Voltage Loop	PLL or Droop Loop	Current Loop	Filter	Time Delay	Stable/ Unstable	Critically Stable (Oscillation)
Refs.[9]-[13]	√					√	*LCL*	√	Accurate	No mention
Ref.[14]	√				√	√	*L*		Accurate	Not Accurate
Ref.[15]	√				√	√	*LCL*	√	Accurate	No mention
Refs.[16]-[17]	√				√	√	*LCL*		Accurate	No mention
Ref.[18]	√		√		√	√	*LC*		Qualitative Description	Qualitative Description
Refs.[19]-[20]		√	√		√		*L*		Accurate	No mention
Refs.[21]-[22]		√	√			√	*LC*		Conservative	No mention
This Paper	√		√	√	√	√	*LCL*		Accurate	Accurate

ence factors are analyzed quantitatively and it is found that the operation points, grid strength, and the interaction of multiple control loops influence the system stability greatly. Furthermore, it is first revealed that the grid impedance has different influence on the system high-frequency and low-frequency stability, and this contradiction can be alleviated through decreasing the PLL bandwidth. Also, the comparison with the conventional analysis method is conducted, which further shows the advantages of the proposed analysis method. Based on these conclusions, some measures are put forward to enhance the stable margin of the PV generators and suppress the low-frequency power oscillation. Finally, all the theoretical analyses are verified by the real-time hardware-in-loop (HIL) tests mainly composed of the RTLAB and TMS320F28335 DSPs.

The brief comparison with the conventional methods is shown in Table I and the main contributions of this paper are summarized as follows.

1) The nonlinear discontinuous P&O-based PV power loop is taken into consideration. Then, some assumptions can be further relaxed, for example, the dc side of the PV generator can be modeled accurately and there is no need to simplify it into an ideal voltage source anymore. Hence, more accurate results especially for the low-frequency oscillation can be obtained.
2) The completeness of the results is improved, and the stable state, unstable state, and critically stable state can be judged accurately. Especially for the critically stable state, the conventional analysis methods are not suitable to analyze it. But the proposed analysis method can explore this critically stable state well, both the oscillation amplitude and frequency can be calculated accurately, which is very beneficial to the relevant quantitative analyses.
3) It is found that the grid impedance (or grid strength) has different influence on the system high-frequency and low-frequency stability. The conventional analysis methods show that the grid impedance is adverse to the stability of the PV generator [9]–[17], where the frequency range is relatively high. However, according to the analysis of this paper, the grid impedance is beneficial to the low-frequency stability.

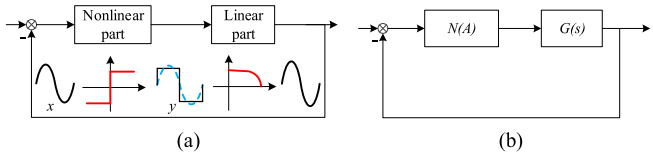

Fig. 1. Schematic of the DF method. (a) Signal flow diagram. (b) Equivalent control block diagram in the frequency domain.

The remainder of this paper is organized as follows. In Section II, the basic principles of the DF method is introduced. In Section III, the complete mathematic model of the *LCL*-Filtered single-stage PV generators connected to weak grid is derived. Then, in Section IV, the detailed stability analysis is conducted and the comparison with the conventional stability analysis method is also made. Subsequently, the validity of the theoretical analyses is demonstrated through HIL tests in Section V. At last, the conclusions are drawn in Section VI.

II. BRIEF INTRODUCTION OF DF METHOD

In this section, the basic principles of the DF method are introduced. DF method was first proposed by Prof. P. J. Daniel in 1940, and it is widely used in the nonlinear analysis field especially for the discontinuous links to analyze the system stability [23], [24]. Being different from the conventional small-signal analysis which is a kind of time-domain approximation methods, the DF method is a kind of frequency-domain approximation methods. The time-domain response of these links is usually discontinuous; hence, they are very difficult to be dealt with in the time domain. However, their frequency-domain response is usually continuous through a reasonable approximation, thus it is possible to deal with them in the frequency domain, which is the basic point of the DF method.

Fig. 1(a) shows the signal flow diagram of the whole system, which contains the nonlinear and linear parts. Through the figure, it can be concluded that if the nonlinear system meets following two requirements.

1) The nonlinear part is odd-symmetric.
2) The linear part is low-pass.

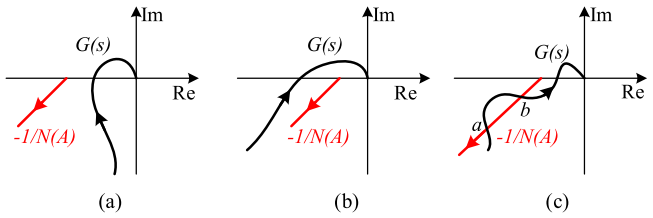

Fig. 2. Modified Nyquist criterion. (a) Stable. (b) Unstable. (c) Critically stable.

Then, only the first harmonic component in the system needs to be considered, because the dc component and higher harmonics are filtered out. The critical step of the DF method is to obtain the first harmonic component of the output when the nonlinear part is excited with sinusoidal signal input. Assuming that the input is $x = A\sin(\omega t)$ and the output is y, which is also a periodic signal. The output y can be expanded according to Fourier series as

$$y = \sum_{k=1}^{\infty} A_k \sin\left(k\omega t + \theta_k\right). \tag{1}$$

Based on (1), the approximate transfer function of the nonlinear part can be obtained by the ratio of the first harmonic component and the input sinusoidal signal. That is

$$N\left(A\right) = \frac{A_1 e^{j\theta_1}}{A} \tag{2}$$

where $N(A)$ is called the DF of the nonlinear part and it usually changes with different amplitude A.

Combining the linear part, the whole nonlinear system can be approximately transformed into a linear system in the frequency domain as shown in Fig. 1(b) where $G(s)$ is the transfer function of the linear part. In the obtained linear system, $N(A)$ can be viewed as a variable gain amplifier. For the linear system in Fig. 1(b), the modified Nyquist criterion can be adopted to judge stability of the system according to the relative position of $-1/N(A)$ and $G(s)$ in the s plane. For the minimum phase system $G(s)$, the modified Nyquist criterion can be expressed as follows.

1) If $-1/N(A)$ is not surround by $G(s)$, the system is stable as shown in Fig. 2(a).
2) If $-1/N(A)$ is surround by $G(s)$, the system is unstable as shown in Fig. 2(b).
3) If $-1/N(A)$ intersects with $G(s)$, the system is critically stable as shown in Fig. 2(c). For the intersection with amplitude A_a, if the system is unstable in the region $[A_a - \Delta A,\ A_a)$ and is stable in the region $(A_a,\ A_a + \Delta A]$ where $\Delta A \ll A_a$, the intersection is the stable oscillation point (persistent oscillation) like the point a. Or else, the intersection is unstable like the point b.

For the non-minimum phase system $G(s)$, the corresponding modified Nyquist criterion can be derived in the similar way. Furthermore, for the stable oscillation point, the oscillation amplitude A_o and frequency ω_o can be calculated as

$$\begin{cases} G_{Im}\left(\omega_o\right) = 0 \\ N\left(A_o\right) = -1/G_{Re}\left(w_o\right) \end{cases} \tag{3}$$

where $G(j\omega) = G_{Re}(\omega) + jG_{Im}(\omega)$.

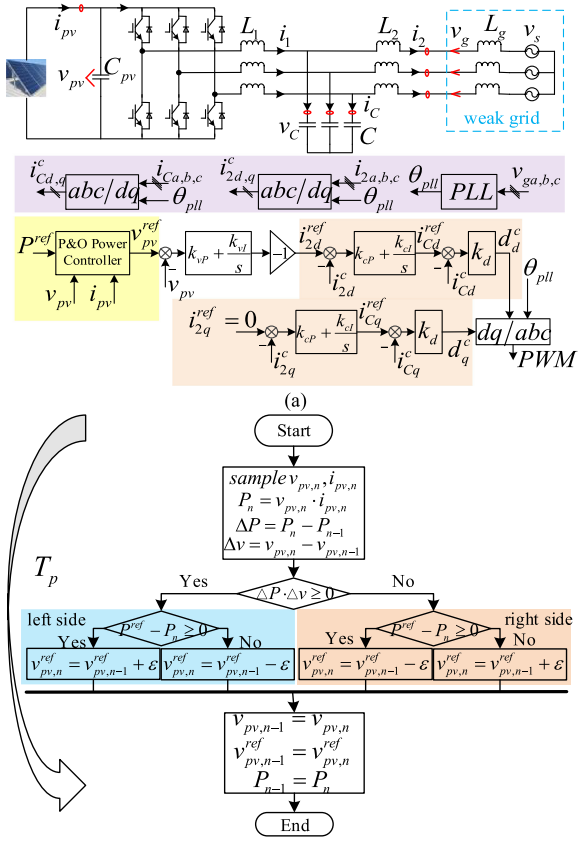

Fig. 3. (a) Typical topology and control strategy for the *LCL*-Filtered single-stage PV generator. (b) Flowchart of P&O based power control.

III. Modeling of *LCL*-Filtered Single-Stage PV Generators

In this section, the complete mathematic model of the *LCL*-Filtered single-stage PV generator is derived in detail. As shown in Fig. 3, the output current and voltage of the PV panel are $i_{\rm pv}$ and $v_{\rm pv}$, respectively, the output of the PV panel is smoothed by the capacitor $C_{\rm pv}$. On the ac side, the *LCL* filter is used to filter the output of the PV generator, the inductance and capacitance of the *LCL* filter are L_1, L_2, and C, respectively. The three-phase inductive currents of L_1 and L_2 are $i_{1a,b,c}$ and $i_{2a,b,c}$, the three-phase capacitive currents and voltages of C are $i_{Ca,b,c}$ and $v_{Ca,b,c}$. The weak grid is simulated through a grid inductor L_g, an ideal three-phase ac voltage source $v_{sa,b,c}$ is connected in the series form, and the terminal voltages of the weak grid are $v_{ga,b,c}$.

The typical P&O-based control strategy is adopted for the *LCL*-Filtered single-stage PV generator. The outermost loop is PV power loop, the middle loop is dc voltage loop, and the inner loop is current loop. The first two loops are unrelated to the PLL, but the last current loop is strongly coupled with the PLL.

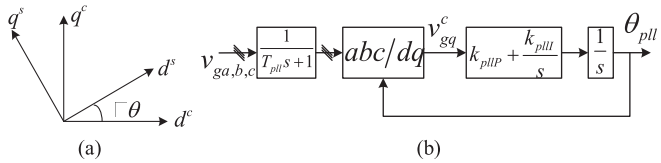

(a) (b)

Fig. 4. (a) Phase of s frame and c frame. (b) Control block diagram of PLL.

For the PV power loop, $i_{\rm pv}$ and $v_{\rm pv}$ are sampled to realize the power regulation, the widely used P&O-based power control is adopted to overcome the intermittency of the solar energy. According to the new grid code regulations, the PV generators must inject the constant power into the grid to provide reserve service and avoid adverse effects like overloading the grid when the penetration of PV generators is high [25]–[26]. The flow chart of P&O-based power control with function of constant power injection is shown in Fig. 3(b), where T_P is the power control cycle and ε is the perturbation size. Through the figure, it can be seen that if $P^{\rm ref}$ is greater than the maximum power of the PV generator, the PV generator outputs the maximum power. If $P^{\rm ref}$ is less than the maximum power of the PV generator, the PV generator outputs the power $P^{\rm ref}$.

For the dc voltage loop, the proportional-integral (PI) controller is adopted to make $v_{\rm pv}$ track $v_{\rm pv}^{\rm ref}$ accurately through regulating the active current.

For the current loop, the conventional grid currents feedback control plus capacitor currents feedback active damping is adopted based on the rotating *d–q* frame, whose *d*-axis is orientated to the weak grid voltage vector. $v_{ga,b,c}$ are the inputs of the PLL for the synchronization and the output of PLL is the observed angular $\theta_{\rm pll}$ of $v_{ga,b,c}$,which is used for the *a-b-c* to *d–q* transformation and its inverse transformation as shown in Fig. 3(a). In addition, to realize the unity power factor, the reference current $i_q^{\rm ref}$ is set as zero with consideration of the direction of the rotating frame.

When the PLL is taken into consideration, the system has two *d–q* frames, namely, the system *d–q* frame and the controller *d–q* frame [27]. The system *d–q* frame is defined by the weak grid voltages $v_{ga,b,c}$, which is identified by superscript "*s*", while the controller *d–q* frame is defined by the PLL, which is identified by superscript "*c*". In the steady state, the controller *d–q* frame is aligned with the system *d–q* frame. However, when the system is disturbed, the position of the two *d–q* frames is changed as shown in Fig. 4(a). The disturbances of the weak grid voltages $v_{ga,b,c}$ propagate to the PLL output angle, and further to the current and duty-ratio vector in the controller *d–q* frame. Hence, the current loop is strongly coupled with the PLL.

For the convenience of small-signal modeling, the state variable x is expressed as the following form uniformly in this paper:

$$x = X^* + \Delta x \tag{4}$$

where X^* is the corresponding equilibrium point, and Δx is the small disturbance.

According to Fig. 3(a), the ac-side model of the *LCL*-Filtered single-stage PV generator can be derived as

$$\begin{cases} L_1\frac{di^s_{1d}}{dt} = \omega L_1 i^s_{1q} + d^s_d v_{\rm pv} - v^s_{cd} \\ L_1\frac{di^s_{1q}}{dt} = -\omega L_1 i^s_{1d} + d^s_q v_{\rm pv} - v^s_{cq} \\ C\frac{dv^s_{cd}}{dt} = \omega C v^s_{cq} + i^s_{1d} - i^s_{2d} \\ C\frac{dv^s_{cq}}{dt} = -\omega C v^s_{cd} + i^s_{1q} - i^s_{2q} \\ (L_2+L_g)\frac{di^s_{2d}}{dt} = \omega(L_2+L_g) i^s_{2q} + v^s_{cd} - v^s_{sd} \\ (L_2+L_g)\frac{di^s_{2q}}{dt} = -\omega(L_2+L_g) i^s_{2d} + v^s_{cq} - v^s_{sq} \end{cases} \tag{5}$$

$$\begin{cases} v^s_{gd} = L_g\frac{di^s_{2d}}{dt} - \omega L_g i^s_{2q} + v^s_{sd} \\ v^s_{gq} = L_g\frac{di^s_{2q}}{dt} + \omega L_g i^s_{2d} + v^s_{sq} \end{cases} \tag{6}$$

where ω is the rated angular frequency.

Then, the small-signal model of the ac side can be obtained as

$$\begin{cases} L_1\frac{d\Delta i^s_{1d}}{dt} = \omega L_1 \Delta i^s_{1q} + D^{s*}_d \Delta v_{\rm pv} + \Delta d^s_d V^*_{\rm pv} \\ L_1\frac{d\Delta i^s_{1q}}{dt} = -\omega L_1 \Delta i^s_{1d} + D^{s*}_q \Delta v_{\rm pv} + \Delta d^s_q V^*_{\rm pv} \\ C\frac{d\Delta v^s_{cd}}{dt} = \omega C \Delta v^s_{cq} + \Delta i^s_{1d} - \Delta i^s_{2d} \\ C\frac{d\Delta v^s_{cq}}{dt} = -\omega C \Delta v^s_{cd} + \Delta i^s_{1q} - \Delta i^s_{2q} \\ (L_2+L_g)\frac{d\Delta i^s_{2d}}{dt} = \omega(L_2+L_g)\Delta i^s_{2q} + \Delta v^s_{cd} \\ (L_2+L_g)\frac{d\Delta i^s_{2q}}{dt} = -\omega(L_2+L_g)\Delta i^s_{2d} + \Delta v^s_{cq} \end{cases} \tag{7}$$

$$\begin{cases} \Delta v^s_{gd} = L_g\frac{d\Delta i^s_{2d}}{dt} - \omega L_g \Delta i^s_{2q} \\ \Delta v^s_{gq} = L_g\frac{d\Delta i^s_{2q}}{dt} + \omega L_g \Delta i^s_{2d}. \end{cases} \tag{8}$$

The state variables x^s in the system *d–q* frame should be transformed into the state variables x^c in the controller *d–q* frame when they are fed back for control. As shown in Fig. 4(a), the relationship between x^s and x^c can be expressed as

$$\begin{aligned} x^c &= e^{j\Delta\theta}x^s = e^{j(\theta-\theta_{\rm pll})}x^s = e^{-j\Delta\theta_{\rm pll}}x^s \\ &= \left[\cos\Delta\theta_{\rm pll} - j\sin\Delta\theta_{\rm pll}\right]x^s \end{aligned} \tag{9}$$

where θ is the actual angle of the system *d–q* frame, and $\theta_{\rm pll}$ is the output angel of PLL. In the steady state, $\theta_{\rm pll} = \theta$ and $\Delta\theta_{\rm pll}$ is the corresponding small disturbance during the transient state. Considering the small disturbance, $\cos\Delta\theta_{\rm pll} \approx 1$, $\sin\Delta\theta_{\rm pll} \approx \Delta\theta_{\rm pll}$, the transformation from Δx^s to Δx^c and its inverse transformation can be obtained as

$$\begin{cases} \Delta x^c_d = \Delta x^s_d + \Delta\theta_{\rm pll} X^{s*}_q \\ \Delta x^c_q = \Delta x^s_q - \Delta\theta_{\rm pll} X^{s*}_d \end{cases} \tag{10}$$

$$\begin{cases} \Delta x^s_d = \Delta x^c_d - \Delta\theta_{\rm pll} X^{c*}_q \\ \Delta x^s_q = \Delta x^c_q + \Delta\theta_{\rm pll} X^{c*}_d \end{cases} \tag{11}$$

where $X^{s*}_q = X^{c*}_q$ and $X^{s*}_d = X^{c*}_d$ in the steady state.

Furthermore, from Fig. 4(b), it can be deduced that

$$\Delta\theta_{\rm pll} = \Delta v^c_{gq}{\rm PI}_{\rm pll}/s = \Delta v^c_{gq}\frac{k_{{\rm pll}P}\,s + k_{{\rm pll}I}}{s^2}. \tag{12}$$

Combining (10), (12) and Fig. 4(b), $\Delta\theta_{\rm pll}$ can be expressed as

$$\Delta\theta_{\rm pll} = \frac{\rm PI_{pll}}{s + V_{gd}^{s*}\rm PI_{pll}} \Delta \frac{1}{T_{\rm pll}s+1} \Delta v_{gq}^{s} \tag{13}$$

where $1/(T_{\rm pll}s+1)$ is used to filter out the high-frequency harmonics of $v_{ga,b,c}$.

At this point, the model of the ac side is established completely. Hereafter, the model of the dc side will be established. As shown in Fig. 3(a), for the dc side, the following equation can be derived:

$$C\frac{dv_{\rm pv}}{dt} = i_{\rm pv} - 1.5\left(d_d^s i_{1d}^s + d_q^s i_{1q}^s\right). \tag{14}$$

Then, the small-signal model of the dc side can be obtained as

$$C\frac{d\Delta v_{\rm pv}}{dt} = g_{\rm pv}\Delta v_{\rm pv} - 1.5 \left(\Delta d_d^s I_{1d}^{s*} + D_d^{s*}\Delta i_{1d}^s + \Delta d_q^s I_{1q}^{s*} + D_q^{s*}\Delta i_{1q}^s\right) \tag{15}$$

where $\Delta i_{\rm pv} = g_{\rm pv}\Delta v_{\rm pv}$. Taking the model of the PV panel into consideration [28], the following equations can be obtained:

$$i_{\rm pv} = N_P\left(I_{\rm sc} + K_I\Delta T\right) \left[\frac{G}{G_N} - \frac{\exp\left(v_{\rm pv}/N_S V_t a\right) - 1}{\exp\left(\left(V_{\rm oc} + K_V\Delta T\right)/V_t a\right) - 1}\right] \tag{16}$$

where N_P and N_S are the numbers of series and parallel modules. $I_{\rm sc}$ and $V_{\rm oc}$ are the open-circuit voltage and short-circuit current of a PV model. V_t is the thermal voltage and a is the ideality constant of the equivalent diode. G and G_N are the actual irradiance and the nominal irradiance, respectively. $\Delta T = T - T_N$, T and T_N are the actual temperature and the nominal temperature, respectively. K_I and K_V are the current and voltage coefficients, respectively. Then, it can be derived that

$$\begin{cases} g_{\rm pv} = \frac{-N_P\left(I_{\rm sc}+K_I\Delta T\right)}{\exp\left(\left(V_{\rm oc}+K_V\Delta T\right)/V_t a\right)-1} \Delta \frac{\exp\left(V_{\rm pv}^*/N_S V_t a\right)}{N_S V_t a} \\ \Delta P = V_{\rm pv}^*\Delta i_{\rm pv} + \Delta v_{\rm pv} I_{\rm pv}^* = K_{\rm pv}\Delta v_{\rm pv} \\ K_{\rm pv} = g_{\rm pv}V_{\rm pv}^* + P^{\rm ref}/V_{\rm pv}^* \end{cases} \tag{17}$$

where ΔP is the small disturbance of the output power of the PV panel.

For controllers related to the dc side, the dc voltage loop is linear and relatively easier. But the outmost P&O-based power loop is nonlinear and discontinuous; it is the critical link and should be modeled properly. Based on Fig. 3(b), the actual output of the P&O-based power controller is shown as the black line in Fig. 5(a); it can be seen that the actual value of $v_{pv}^{\rm ref}$ is stair-stepping. Considering that T_P is very small, the output can be expressed approximately as

$$v_{\rm pv}^{\rm ref} = \frac{\varepsilon}{T_P}\int \rm sgn\left(P^{\rm ref} - P_n\right) sgn\left(\Delta P\right) sgn\left(\Delta v\right) dt \tag{18}$$

where $\rm sgn(x)$ is the sign function. If $x \geq 0$, $\rm sgn(x) = 1$. If $x < 0$, $\rm sgn(x) = -1$. The approximate value of $v_{\rm pv}^{\rm ref}$ based on (18) is shown as the red line in Fig. 5(a).

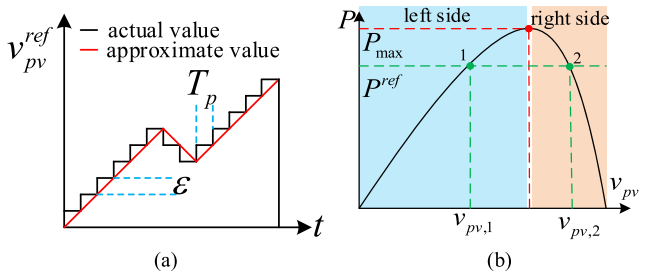

Fig. 5. (a) Output of P&O based power control. (b) Power-voltage curve of the PV panel.

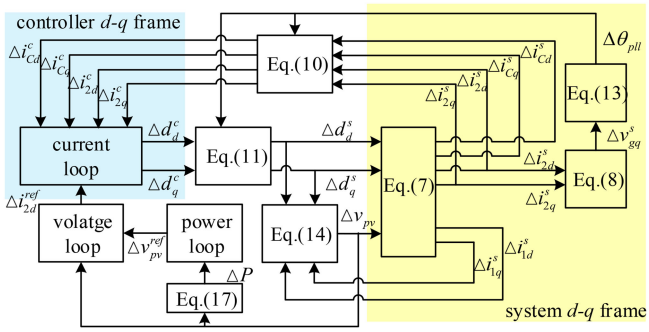

Fig. 6. Signal flow diagram of the whole *LCL*-Filtered single-stage PV generator.

Furthermore, through the power-voltage curve of the PV panel shown in Fig. 5(b), the following equations can be obtained if sampling errors are ignored:

$$\begin{cases} \rm sgn\left(\Delta P\right) sgn\left(\Delta v\right) = 1, & \text{left side} \\ \rm sgn\left(\Delta P\right) sgn\left(\Delta v\right) = -1, & \text{rigth side.} \end{cases} \tag{19}$$

Therefore, (18) can be simplified as

$$\begin{cases} v_{\rm pv}^{\rm ref} = \frac{\varepsilon}{T_P}\int \rm sgn\left(P^{\rm ref} - P_n\right) dt, & \text{left side} \\ v_{\rm pv}^{\rm ref} = \frac{-\varepsilon}{T_P}\int \rm sgn\left(P^{\rm ref} - P_n\right) dt, & \text{rigth side.} \end{cases} \tag{20}$$

Through (14) and (20), the dc-side dynamics and the P&O-based power control are modeled properly. Their influence on the system stability can be taken into consideration based on the DF method, which will be illustrated in detail in the next section.

Based on (5), (14), and (17), choosing $V_{\rm pv}^*$ and P^* (namely $P^{\rm ref}$) as known variables, the other related equilibrium points can be calculated as

$$\begin{cases} V_{gq}^{s*} = 0 \\ V_{gd}^{s*} = \sqrt{\left(\left(1.5V\right)^2 + \sqrt{\left(1.5V\right)^4 - \left(3P^*\omega L_g\right)^2}\right)/4.5} \\ I_{2q}^{s*} = 0, I_{2d}^{s*} = P^*/\left(1.5V_{gd}^{s*}\right) \\ I_{1q}^{s*} = \omega \rm C V_{gd}^{s*}, I_{1d}^{s*} = I_{2d}^{s*} - \omega^2 \rm C L_2 I_{2d}^{s*} \\ I_{Cq}^{s*} = I_{1q}^{s*}, I_{Cd}^{s*} = I_{1d}^{s*} - I_{2d}^{s*} \\ D_q^{s*} = \frac{\omega L_2 I_{2d}^{s*} + \omega L_1 I_{1d}^{s*}}{V_{\rm pv}^*}, D_d^{s*} = \frac{V_{gd}^{s*} - \omega L_1 I_{1q}^{s*}}{V_{\rm pv}^*} \end{cases} \tag{21}$$

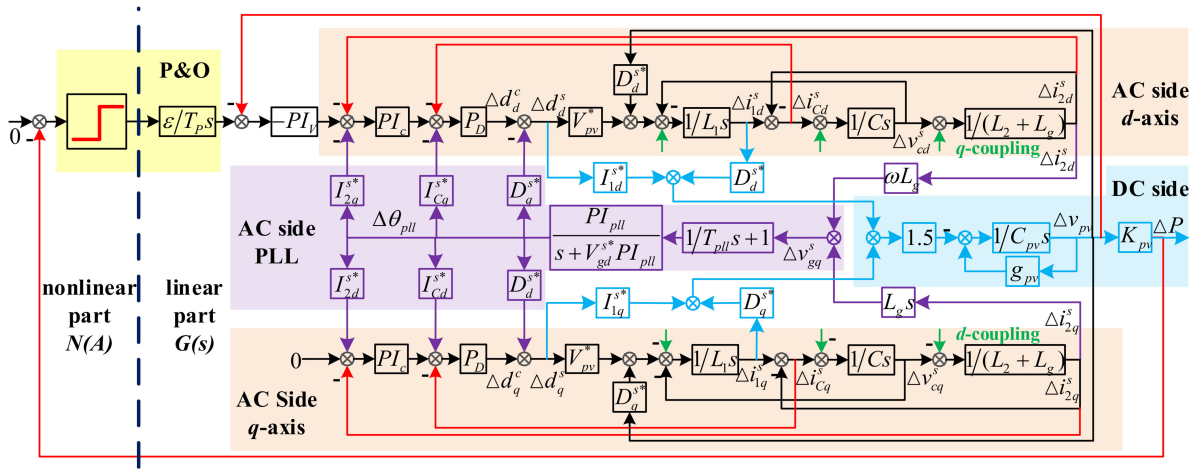

Fig. 7. Complete model of the *LCL*-Filtered single-stage PV generator.

where V is the amplitude of the ideal ac voltage sources $v_{sa,b,c}$ in Fig. 3(a).

Since the signals of the whole *LCL*-Filtered single-stage PV generator is numerous and complexly linked, Fig. 6 shows the signal flow diagram of the whole system based on Fig. 3(a) to help clarify the cause and effect.

Based on Fig. 6 and combining (7), (8), (10), (11), (13), (14), and (17), the complete and detailed model of the *LCL*-Filtered single-stage PV generator is presented in Fig. 7 when the operation point is located on the left-hand side, where the *d*–*q* coupling terms are not presented for the compactness. The model when the operation point is located on the right-hand side can be derived in the similar way. From the figure, it can be seen that when the P&O-based power control is taken into consideration, the whole system can be divided into two parts namely the nonlinear part and the linear part. For the nonlinear part, it is discontinuous and the conventional small-signal modeling cannot be applied anymore. However, this structure is the same as Fig. 2(a); hence, it is suitable to be analyzed through the DF method as introduced in Section II. Furthermore, it should be noted that the complete model of the *LCL*-Filtered single-stage PV generator meets the two requirements of DF method.

1) The nonlinear part namely the sign function is odd-symmetric.
2) The linear part is low-pass because of the control loops and the *LCL* filter.

IV. Detailed Stability Analysis

In this section, the stability analysis is conducted in detail and the corresponding influence factors are carefully studied. Based on the obtained results, some measures to enhance the system stability are summed up. Before the detailed stability analysis, the DF $N(A)$ of the sign function should be calculated. According to definition of DF as shown in (2), the DF $N(A)$ of the sign function can be easily calculated as

$$N(A) = \frac{4}{\pi A}. \tag{22}$$

Also, the comparison with the conventional stability analysis method is made. The conventional stability analysis method is based on the linear system theory, whose maximum research scope is from $\Delta v_{\rm pv}^{\rm ref}$ to $\Delta v_{\rm pv}$ as shown in Fig. 8. The whole analysis procedures are similar to the procedures presented in [9]–[17], namely obtaining corresponding results through open-loop (or close-loop) Bode diagrams. Compared to Fig. 7, it can be found that the whole PV power loop is out of consideration in the conventional stability analysis method.

The used PV module in this paper is KC200GT, whose detailed parameters are introduced in [28]. The whole PV panel consists of 15 parallel and 60 series KC200GT PV modules, then the maximum power of the PV panel can reach about 190 kW and the corresponding voltage $v_{\rm pv}$ is about 1680 V under the nominal irradiance $G_N = 1000$ W/m^2 and the nominal temperature $T_N = 298.16$ K. The other rated electrical and control parameters of the *LCL*-Filtered single-stage PV generator are shown in Table II, where the operation point is indicated by $(V_{\rm pv}^*,\ P^*)$ and the other equilibrium points can be derived through (21).

A. Operation Points

In this part, the operation points of the PV panel are studied, where the other parameters are kept the same as Table II except for the operation points and their dependent parameters $g_{\rm pv}$, $K_{\rm pv}$. Fig. 9 shows the influence of operation points on the system stability analyzed by the proposed analysis method. Fig. 9(a) shows the system Nyquist diagrams when the operation points are on the left-hand side of the power-voltage curve of the PV panel shown in Fig. 5(b), while Fig. 9(b) shows system Nyquist diagrams when operation points are on the right-hand side.

According to the modified Nyquist criterion of the DF method, it can be concluded that the system is critically stable when the operation points are on the left-hand side. While under the same output power, the system is stable when the operationpoints are on the right-hand side. Furthermore, from Fig. 9(a), it can be seen that with the operation points further moving toward the left-hand side, the oscillation amplitude is obviously increased. According to (3), the specific oscillation

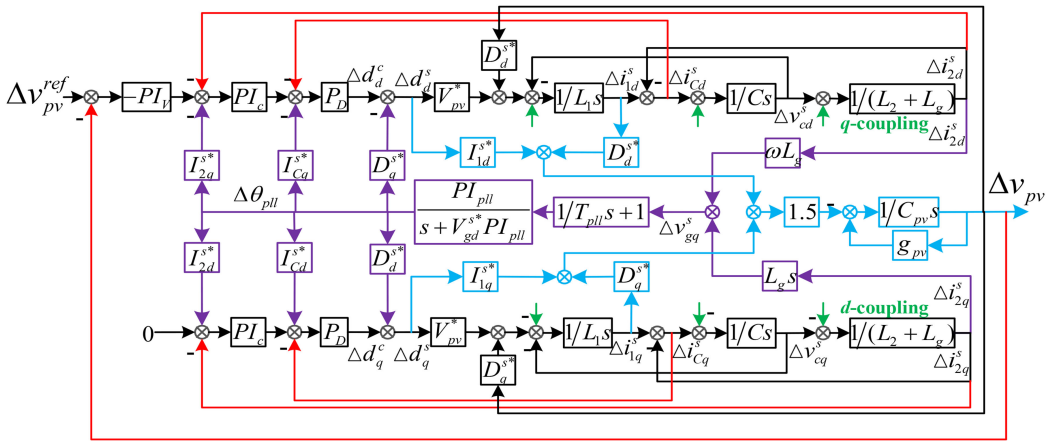

Fig. 8. Research scope of the conventional stability analysis method.

TABLE II
RATED SYSTEM PARAMETERS

Parameters	Rated Value
V, ω	311 V, 100π rad/s
L_g	0.2 mH
L_1, C, L_2	1.8 mH, 20 μF, 0.9 mH
C_{pv}	2 mF
G, T	1000 W/m^2 (G_N), 298.16 K (T_N)
(V_{pv}^*, P^*)	(1220 V, 150 kW)
g_{pv}	-8×10^{-4} A/V
K_{pv}	121.7 W/V
PV Power Loop	ε = 1V, T_P = 0.2 ms
DC Voltage Loop	k_{vP} = 0.2 A/V, k_{vI} = 100 A/Vs
Current Loop	k_{cP} = 1.2 , k_{cI} = 500 s^{-1} k_d = 0.01 V/A
PLL	k_{pllP} = 0.45 rad/Vs, k_{pllI} = 8 rad/Vs^2 T_{pll} = 10 μs

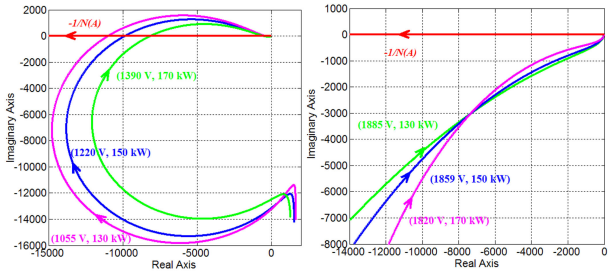

Fig. 9. System dynamics with changes of operation points analyzed by the proposed analysis method. (a) Left-Side operation points. (b) Right-Side operation points.

amplitude and frequency can be calculated as

$$\begin{cases} A_o = 10.5 \text{ kW} \\ f_o = 23 \text{ Hz} \end{cases}, (1390 \text{ V}, \ 170 \text{ kW})$$

$$\begin{cases} A_o = 12.4 \text{ kW} \\ f_o = 23.8 \text{ Hz} \end{cases}, (1220 \text{ V}, \ 150 \text{ kW})$$

$$\begin{cases} A_o = 13.8 \text{ kW} \\ f_o = 25.1 \text{ Hz} \end{cases}, (1055 \text{ V}, \ 130 \text{ kW}) \qquad (23)$$

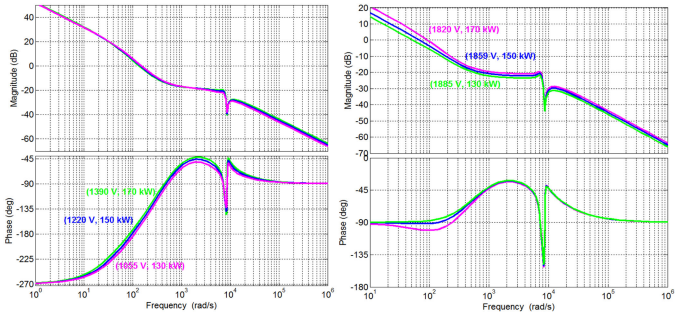

Fig. 10. System dynamics with changes of operation points analyzed by the conventional analysis method. (a) Left-Side operation points. (b) Right-Side operation points.

where the angular frequency ω_o has been transformed into frequency f_o for convenient comparison.

Through (23), it can be found that the changes of operation points on the left-hand side will greatly influence the oscillation amplitude, but have little influence on the oscillation frequency. It should be noted that the changes of the oscillation amplitude under different left-side operation points are not caused by the coefficient $K_{\mathrm{pv}}(\Delta P = K_{\mathrm{pv}}\Delta v_{\mathrm{pv}})$ since the coefficient K_{pv} under these operation points is almost the same. Instead, the changes of the oscillation amplitude are mainly caused by the system stability.

In conclusion, the right-side operation points can greatly enhance the system stability compared with the left-side operation points.

Fig. 10 shows the influence of operation points on the system stability analyzed by the conventional analysis method. According to Fig. 8, the open-loop Bode diagrams of the system when the operation points are on the left side is presented Fig. 10(a) and the open-loop Bode diagrams of the system when the operation points are on the right side is presented Fig. 10(b).

It should be noted that when the operation points are on the left side, the open-loop transfer function in Fig. 10 is the non-minimum phase system and it contains the one right-half-plane pole. Hence, the conventional stable margin cannot be applied

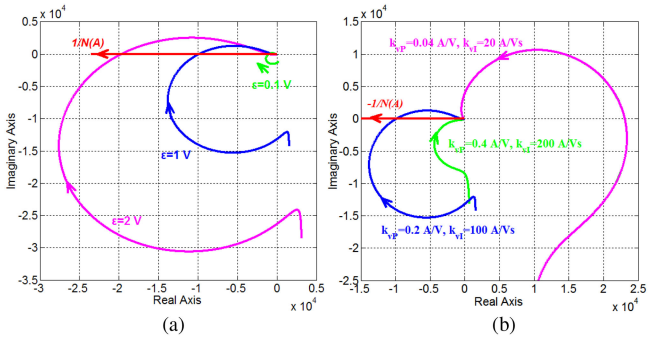

Fig. 11. System dynamics with changes of control parameters analyzed by the proposed analysis method. (a) PV power loop changes where $\varepsilon = 0.1,\ 1,\ 2$ V, respectively. (b) DC voltage loop changes where $k_{vP} = 0.4,\ 0.2,\ 0.04$ A/V and $k_{vI} = 200,\ 100,\ 20$ A/Vs, respectively.

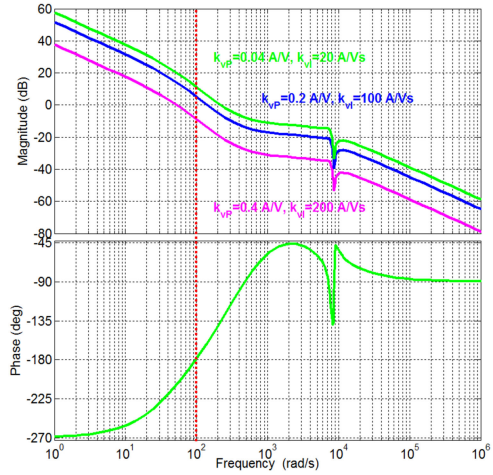

Fig. 12. System dynamics with changes of control parameters analyzed by the conventional analysis method, where $k_{vP} = 0.4,\ 0.2,\ 0.04$ A/V and $k_{vI} = 200,\ 100,\ 20$ A/Vs, respectively.

here too. Based on this fact, through Fig. 10(a), we can only conclude that the system is stable when the operation points are on the left side. This conclusion is not consistent with the conclusion of our proposed analysis method. However, according to the experimental results, it is found that the conclusion of our proposed analysis method is more accurate.

Through Fig. 10(b), it can be seen that the *LCL*-Filtered single-stage PV generator is stable when the operation points are on the right side, which is consistent with the conclusion of our proposed analysis method.

B. Control Loops

The interaction of different control loops will influence the system stability, which will be studied in detail in this part. Except for the studied control parameters which would be changed intentionally, the other parameters are kept the same as Table II. Compared to the PV power loop and the dc voltage loop, the current loop has higher bandwidth and is very fast. Therefore, the current loop has little influence on the low-frequency instability of the *LCL*-Filtered single-stage PV generator. Then, the PV power loop and the dc voltage loop are the main research objects, whose influence on the system stability analyzed by the proposed analysis method is shown in Fig. 11. On the other hand, the PLL is strongly related to the grid strength and they will be studied together in the next part.

According to the proposed analysis method, Fig. 11(a) shows the system Nyquist diagrams when the perturbation size ε of the PV power loop changes from 0.1 to 2 V. When ε increases which means the equivalent bandwidth of the PV power loop increases, the oscillation is more and more obvious. When $\varepsilon = 0.1$ V, the oscillation is very small and can be omitted. But when $\varepsilon = 2$ V, the oscillation is much stronger compared to $\varepsilon = 1$ V, the specific oscillation amplitude and frequency are

$$\begin{cases} A_o = 24.8 \text{ kW} \\ f_o = 24 \text{ Hz} \end{cases}, \varepsilon = 2 \text{ V}. \tag{24}$$

Compared to the results when $\varepsilon = 1$ V shown in (23), the oscillation amplitude is obviously increased but the oscillation frequency changes slightly.

Fig. 11(b) shows the system Nyquist diagrams when the bandwidth of the dc voltage loop varies. The bandwidth of the dc voltage loop is changed through simply scaling the proportional coefficient k_{vP} and the integral coefficient k_{vI} at the same time, that is, the overall gain of the dc voltage controller is changed. As shown in Fig. 11(b), when the gain of the dc voltage controller is expended to 2 times namely $k_{vP} = 0.4$ A/V and $k_{vI} = 200$ A/Vs, the system is stable as the green Nyquist curve shows. But when the gain of the dc voltage controller is reduced to 1/5 namely $k_{vP} = 0.04$ A/V and $k_{vI} = 20$ A/Vs, the system becomes unstable as the pink Nyquist curve shows, where although $G(s)$ does not surround $-1/N(A)$, but $G(s)$ has poles on the right-half plane.

Therefore, it can be concluded that the system is more stable if the bandwidth of the PV power loop is lower and the bandwidth of the dc voltage loop is higher.

Fig. 12 shows the influence of control parameters on the system stability analyzed by the conventional analysis method. Since the conventional analysis method cannot take the nonlinear discontinuous PV power loop into consideration, the influence of the whole PV power loop is out of consideration, and only the influence of the dc voltage loop is studied. From this point, it can be seen that the proposed stability analysis method has obvious advantages than the conventional stability analysis method. More loops and more influence factors can be taken into consideration, hence more accurate results especially for the low-frequency oscillation can be obtained.

Being similar to Fig. 10, the open-loop transfer function in Fig. 12 is the non-minimum phase system and it contains one right-half-plane pole when the operation points are on the left side. Combining this fact, through Fig. 12, it can be concluded that when the gain of the dc voltage controller is reduced to 1/5 namely $k_{vP} = 0.04$ A/V and $k_{vI} = 20$ A/Vs, the system is unstable, which is consistent with the conclusion of our proposed analysis method. However, when the PI coefficients are that $k_{vP} = 0.2$ A/V, $k_{vI} = 100$ A/Vs (rated) and $k_{vP} = 0.4$ A/V, $k_{vI} = 200$ A/Vs (2 times), it can be only

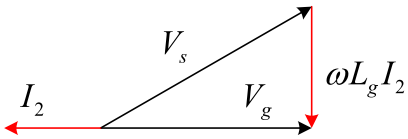

Fig. 13. Phasor diagram in the terminal of the weak grid.

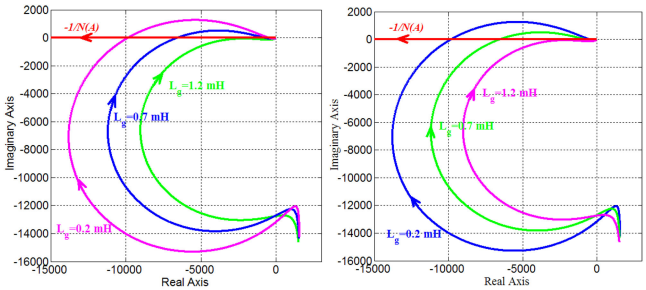

Fig. 14. System dynamics with changes of PLL bandwidth and grid strength analyzed by the proposed analysis method. (a) $L_g = 0.2,\ 0.7,\ 1.2$ mH when $k_{\mathrm{pll}P} = 0.45$ rad/Vs, $k_{\mathrm{pll}I} = 8$ rad/Vs^2. (b) $L_g = 0.2,\ 0.7,\ 1.2$ mH when $k_{\mathrm{pll}P} = 2.25$ rad/Vs, $k_{\mathrm{pll}I} = 40$ rad/Vs^2.

obtained that the system is stable. The critically stable state when $k_{vP} = 0.2$ A/V and $k_{vI} = 100$ A/Vs (rated) cannot be reflected obviously, which shows that the accuracy of the conventional stability analysis method is limited compared to our proposed analysis method.

C. Grid Strength and PLL

In this part, the influence of grid strength and PLL is studied, where the other parameters are kept the same as Table II except for the chosen parameters. Due to the existence of L_g which represents the grid strength, the terminal voltages $v_{ga,b,c}$ of the weak grid which are the inputs of the PLL for the synchronization will contain a lot of high-frequency harmonics $(L_g \frac{di_2}{dt})$ as shown in (6) and (8). Therefore, the performance of the PLL will be distorted and the system stability is degraded. In addition, the output power of the PV generator is limited. As shown in Fig. 13, because of the limitation of unity power factor, $\overrightarrow{I_2}$ and $\overrightarrow{V_g}$ are in the opposite direction. The terminal voltage $\overrightarrow{V_g}$, the inductive voltage $j\omega L_g \overrightarrow{I_2}$ and the ideal ac voltage sources $\overrightarrow{V_s}$ constitute a triangle. Thus, the following constraint equation can be obtained

$$\mathrm{PL}_g < 0.75 \frac{V^2}{\omega} \tag{25}$$

where V is the amplitude of $v_{sa,b,c}$. The above constraint (25) can be also obtained from (21).

Under the constraint (25), the allowable maximum L_g is 1.54 mH when the output power is 150 kW, otherwise the system does not have equilibrium points. Within this variation range of L_g, Fig. 14 shows the influence of the PLL bandwidth and grid strength on the system stability analyzed by the proposed analysis method. Fig. 14(a) and (b) show the system Nyquist diagrams with changes of L_g when the PLL bandwidth is different. The PLL bandwidth is changed through simply scaling

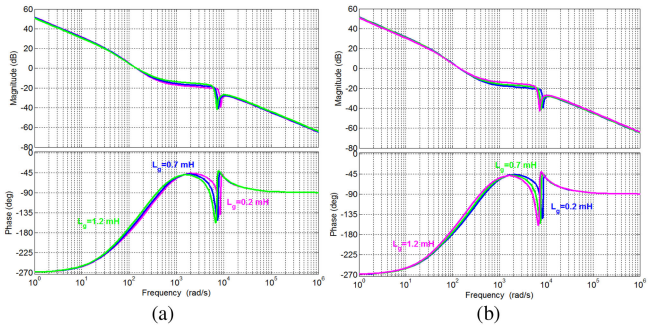

Fig. 15. System dynamics with changes of PLL bandwidth and grid strength analyzed by the conventional analysis method. (a) $L_g = 0.2, 0.7, 1.2$ mH when $k_{\mathrm{pll}P} = 0.45$ rad/Vs, $k_{\mathrm{pll}I} = 8$ rad/Vs^2. (b) $L_g = 0.2, 0.7, 1.2$ mH when $k_{\mathrm{pll}P} = 2.25$ rad/Vs, $k_{\mathrm{pll}I} = 40$ rad/Vs^2.

the proportional coefficient $k_{\mathrm{pll}P}$ and the integral coefficient $k_{\mathrm{pll}I}$ at the same time, that is, the overall gain of the PLL controller is changed. The gain of the PLL controller in Fig. 14(a) is the rated value, while the gain of the PLL controller in Fig. 14(b) is increased to 5 times, where $k_{\mathrm{pll}P} = 2.25$ rad/Vs, $k_{\mathrm{pll}I} = 40$ rad/Vs^2.

As shown in Fig. 14(a), under the condition of low PLL bandwidth, the increase of L_g is beneficial to suppress the low-frequency oscillation. The oscillation amplitude is reduced obviously when L_g is increased to 0.7 mH, furthermore, the system becomes stable and the oscillation is completely suppressed when L_g is increased to 1.2 mH.

However, if the PLL bandwidth is high, the increase of L_g is adverse to the system stability. As shown in Fig. 14(b) where the gain of the PLL controller is increased to 5 times, when L_g is increased to 1.2 mH, the system is unstable. Although $G(s)$ does not surround $-1/N(A)$, $G(s)$ has poles on the right-half plane when L_g equals to 1.2 mH. This is because when the PLL bandwidth is high, the high-frequency stability is dominated. And the high-frequency stability is reduced with the increase of L_g, which has been well explored in [9]–[17]. However, even for the high-frequency stability, the low PLL bandwidth can also increase the maximum acceptable ability for the grid inductor L_g.

In conclusion, the influence of grid strength and PLL is strongly coupled and it is not unidirectional. At the same time, there is a contradiction between the high-frequency stability and the low-frequency stability with the increase of L_g. If the PLL bandwidth is low which means that the low-frequency stability is dominated, the increase of L_g (namely the weaker grid) is beneficial to the system stability. No matter the high-frequency stability or the low-frequency stability, the low PLL bandwidth is always beneficial to the stability of the *LCL*-Filtered single-stage PV generator when it is connected to the weak grid.

Fig. 15 shows the influence of the PLL bandwidth and grid strength on the system stability analyzed by the conventional analysis method. According to Fig. 8, the open-loop Bode diagrams of the system with low PLL bandwidth is presented in Fig. 15(a) and the open-loop Bode diagrams of the system with high PLL bandwidth is presented in Fig. 15(b).

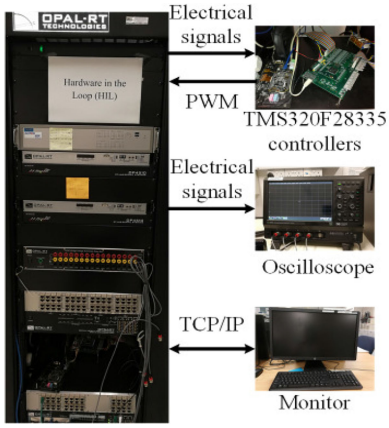

Fig. 16. HIL platform setup.

For Fig. 15(a), the open-loop transfer function is the non-minimum phase system and it only contains one right-half-plane pole. Based on this fact, it can be concluded that the system is stable. But the critically stable state and its variation trend cannot be reflected, while the critically stable state and its variation trend can be well reflected through our proposed stability analysis method as shown in Fig. 14(a). And from the experimental results, it can be found that the conclusion of our proposed analysis method is more accurate. Hence, our proposed analysis method is more advanced than the conventional stability analysis method.

For Fig. 15(b), when $L_g = 0.2, 0.7$ mH, the open-loop transfer function is the non-minimum phase system and it only contains one right-half-plane pole. Therefore, it can be concluded that the system is stable. Similarly, the conclusion about the critically stable state cannot be obtained directly, which shows the limitation of the conventional stability analysis method. However, when $L_g = 1.2$ mH, the open-loop transfer function is the non-minimum phase system and it contains three right-half-plane poles. Combining this fact, it can be concluded that the system is unstable, which is consistent with the conclusion of our proposed analysis method.

V. HIL Tests

To verify the theoretical analyses, the corresponding HIL tests are conducted, whose setup is shown in Fig. 16. The topology and the control method of the *LCL*-Filtered single-stage PV generator are shown in Fig. 3, the related parameters are kept the same as Table II except for the studied parameters in different cases.

Fig. 17 shows the responses of the *LCL*-Filtered single-stage PV generator when the operation points are changed on the left side of the power-voltage curve of the PV panel, in which $\Delta P = P - 150$ kW, $\Delta v_{\rm pv} = v_{\rm pv} - 1200$ V and $\Delta f = f - 50$ Hz. From Fig. 17(a) which shows the output power, PV voltage and output frequency of PLL, it can be seen that the persistent oscillation is existed when the operation points are located on the left side. Furthermore, with the operation points moving left from (1390 V, 170 kW) to (1055 V, 130 kW), the oscillation amplitude becomes larger. These phenomena are

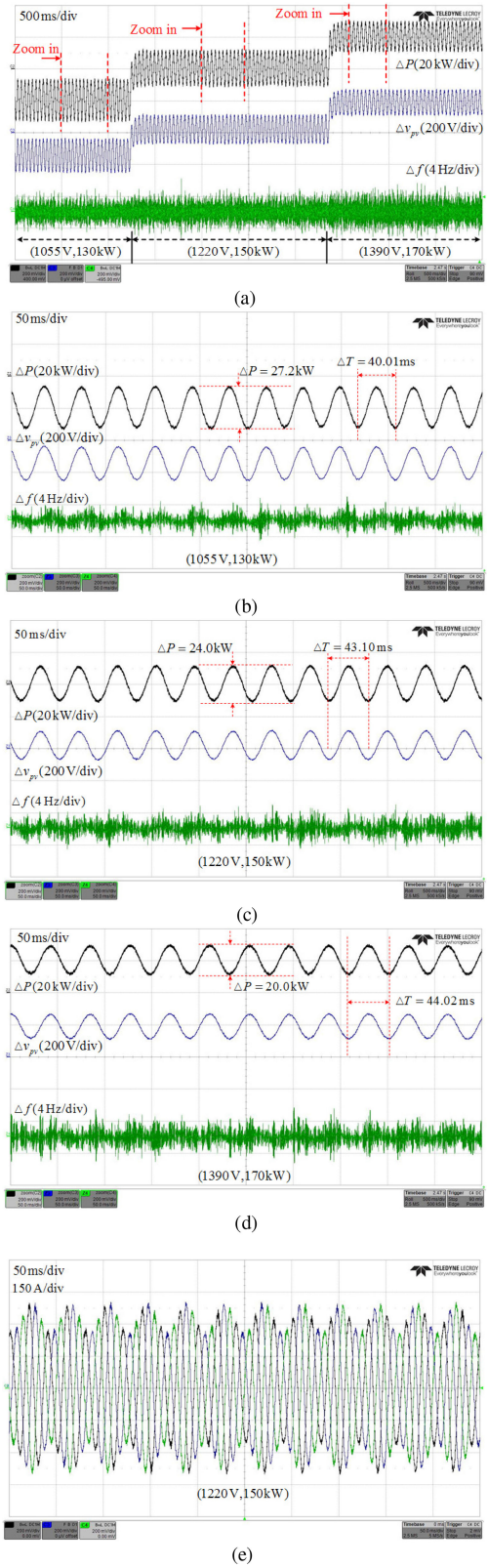

Fig. 17. System responses with changes of left-side operation points. (a) Output power, PV voltage and output frequency of PLL when operation points are (1055 V, 130 kW), (1220 V, 150 kW) and (1390 V, 170 kW) respectively. (b) Enlarged version when the operation point is (1055 V, 130 kW). (c) Enlarged version when the operation point is (1220 V, 150 kW). (d) Enlarged version when the operation point is (1390 V, 170 kW). (e) Output three-phase currents when the operation point is (1220 V, 150 kW).

consistent with the corresponding theoretical analysis of Part A in Section IV. In addition, due to the existence of the grid inductor L_g, the input of PLL contains numerous high-frequency components because of the inductive voltage $L_g \frac{di_2}{dt}$. Hence, the observed frequency has a lot of glitches shown in the figure.

Fig. 17(b) shows the enlarged version when the operation point is (1055 V, 130 kW). As the figure shows, the measured oscillation amplitude and frequency are 13.6 kW and 25 Hz. Then, Fig. 17(c) shows the enlarged version when the operation point is (1220 V, 150 kW) namely the rated operation point, in which the measured oscillation amplitude and frequency are 12 kW and 23.2 Hz. Finally, Fig. 17(d) shows the enlarged version when the operation point is (1390 V, 170 kW), in which the measured oscillation amplitude and frequency are 10 kW and 22.7 Hz. These three results meet the theoretical calculation in (23) well, which can well verify the accuracy and effectiveness of the proposed stability analysis method. At the same time, through the enlarged versions, it can be observed that the output frequency of PLL has obvious low-frequency components except for the high-frequency glitches. However, through the conventional stability analysis method shown in Fig. 10, these oscillation phenomena cannot be analyzed effectively. Hence, it can be effectively proven that our proposed stability analysis method is more accurate than the conventional stability analysis method.

Fig. 17(e) presents the output three-phase currents of the *LCL*-Filtered single-stage PV generator when the operation point is (1220 V, 150 kW) namely the rated operation point. From the figure, it can be seen that the output currents are fluctuated obviously with the low frequency. The rated amplitude of the currents is about 321.5 A under the output power 150 kW, due to the oscillation, the actual amplitude of the currents can reach about 405 A as shown in the figure. Therefore, the efficiency and reliability of the power electronic devices are greatly influenced because of the increased thermal loss and current stress.

Fig. 18 presents the responses of the *LCL*-Filtered single-stage PV generator when the operation points are changed on the right side of the power-voltage curve of the PV panel, in which $\Delta P = P - 150$ kW, $\Delta v_{\rm pv} = v_{\rm pv} - 1800$ V and $\Delta f = f - 50$ Hz. Fig. 18(a) shows the output power, PV voltage and output frequency of PLL when operation points are (1885 V, 130 kW), (1859 V, 150 kW) and (1820 V, 170 kW) respectively. Compared to Fig. 17(a), it can be found that the system is completely stable and there is no obvious low-frequency oscillation in the figure, which shows that the system stability is enhanced when the operation points are located on the right side. This conclusion is also obtained by the conventional stability analysis method.

Fig. 18(b) shows output three-phase currents of the *LCL*-Filtered single-stage PV generator when the operation point is (1859 V, 150 kW). Under the same output power, the output currents in Fig. 18(b) are much smoother than the output currents in Fig. 17(e) and there is no obvious fluctuation.

Fig. 19 shows the responses of the *LCL*-Filtered single-stage PV generator with changes of control loops, where $\Delta P = P - 150$ kW, $\Delta v_{\rm pv} = v_{\rm pv} - 1200$ V and $\Delta f = f - 50$ Hz. Fig. 19(a) shows the output power, PV voltage and output frequency of PLL when $=$ 0.1, 1, 2 V. From the figure, it can

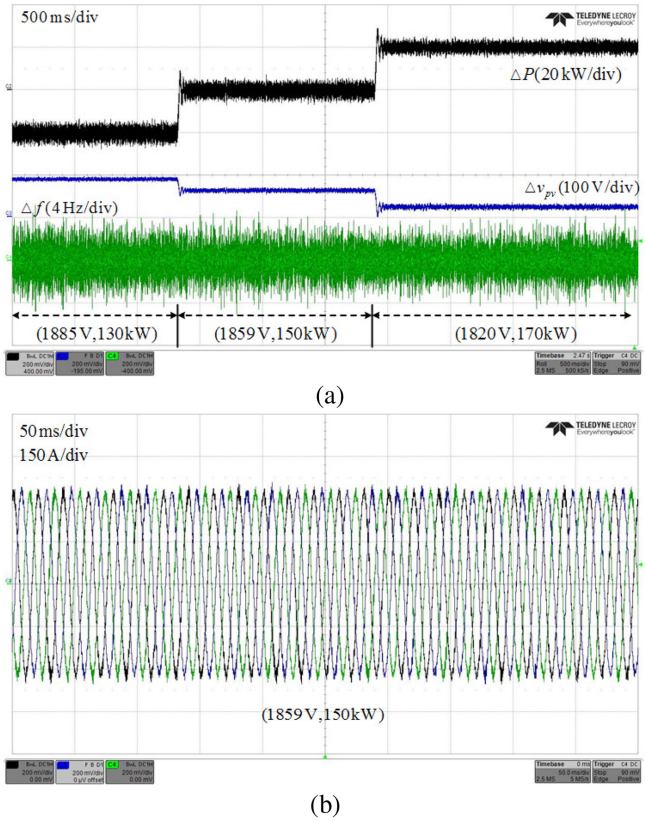

Fig. 18. System responses with changes of right-side operation points. (a) Output power, PV voltage, and output frequency of PLL when operation points are (1885 V, 130 kW), (1859 V, 150 kW), and (1820 V, 170 kW) respectively. (b) Output three-phase currents when the operation point is (1859 V, 150 kW).

be seen that perturbation size ε has great influence on the low-frequency oscillation. With the increase of ε, which means the equivalent bandwidth of the PV power loop is increased, the oscillation is more and more obvious. When $=$ 0.1 V, the oscillation is very small and can be omitted. Then, when $=$ 1 V, the oscillation is obvious. Finally, when $=$ 2 V, the oscillation amplitude is significantly increased. Fig. 19(b) shows the enlarged version when $=$ 2 V. From the figure, the measured oscillation amplitude and frequency are 23.5 kW and 23 Hz. Compared to Fig. 17(c) that shows the situation when $=$ 1 V, the oscillation amplitude is increased to 2 times but the oscillation frequency changes slightly. These phenomena meet the theoretical analysis of Part B in Section IV. Since the conventional stability analysis method has no ability to consider the nonlinear discontinuous PV power loop, the influence of perturbation size ε cannot be studied. This comparison can further illustrate the advantages of our proposed analysis method.

Fig. 19(c) presents the output currents when $=$ 2 V. Since the oscilloscope only has two channels, currents of phase *a* and *b* are monitored and current of phase *c* is not monitored. From the figure, it can be seen that currents are fluctuated violently and the actual amplitude of the currents can reach about 450 A, which exceeds the rated value (321.5 A) about 128.5 A.

Fig. 19(d) shows the output power, PV voltage and output frequency of PLL with different gains of the dc voltage controller, that is, the equivalent bandwidth of the dc volt-

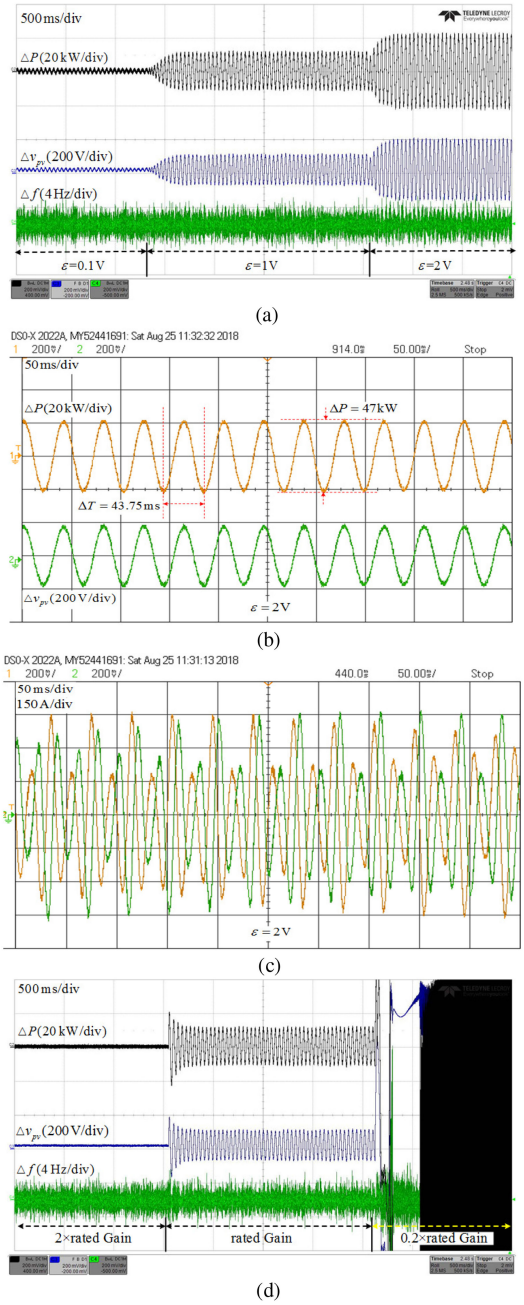

Fig. 19. System responses with changes of control loops. (a) Output power, PV voltage and output frequency of PLL when $\varepsilon = 0.1$, 1, 2 V. (b) Enlarged version when $\varepsilon = 2$ V. (c) Output currents when $\varepsilon = 2$ V. (d) Output power, PV voltage and output frequency of PLL when $k_{vP} = 0.4,\ 0.2,\ 0.04$ A/V and $k_{vI} = 200,\ 100,\ 20$ A/Vs namely 2 × rated gain, rated gain, 0.2 × rated gain of the dc voltage controller, respectively.

age loop is changed. When the gain of the dc voltage controller is 2 times of the rated gain namely $k_{vP} = 0.4$ A/V and $k_{vI} = 200$ A/Vs, the system is completely stable and the low-frequency oscillation is suppressed effectively. But when the gain of the dc voltage controller becomes 1/5 of the rated gain namely $k_{vP} = 0.04$ A/V and $k_{vI} = 20$ A/Vs, the system becomes unstable. Except the critically stable state, these stable and unstable states can be also predicted by the conventional stability analysis method. These experimental results are in

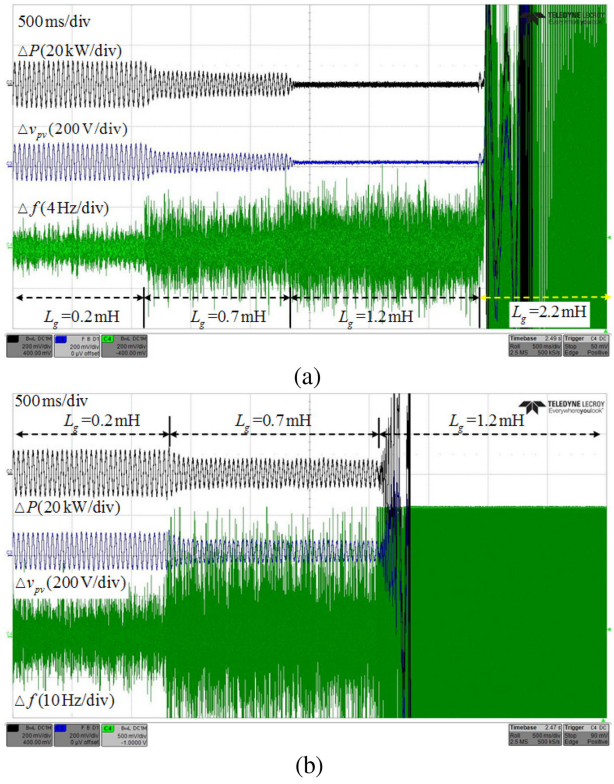

Fig. 20. System responses with changes of grid strength under the different PLL bandwidths. (a) Output power, PV voltage and output frequency of PLL with $L_g = 0.2$, 0.7, 1.2, 2.2 mH when $k_{\mathrm{pll}P} = 0.45$ rad/Vs, $k_{\mathrm{pll}I} = 8$ rad/Vs^2. (b) Output power, PV voltage and output frequency of PLL with $L_g = 0.2$, 0.7, 1.2 mH when $k_{\mathrm{pll}P} = 2.25$ rad/Vs, $k_{\mathrm{pll}I} = 40$ rad/Vs^2.

accordance with the corresponding theoretical analysis of Part B in Section IV.

From Fig. 19, it can be concluded that with the slower outer loop (PV power loop) and the faster inner loop (dc voltage loop), the *LCL*-Filtered single-stage PV generator is easier to be stable.

Fig. 20 shows the responses of the *LCL*-Filtered single-stage PV generator with changes of the grid strength and PLL, where $\Delta P = P - 150$ kW, $\Delta v_{\mathrm{pv}} = v_{\mathrm{pv}} - 1200$ V and $\Delta f = f - 50$ Hz. In Fig. 20(a), the bandwidth of PLL is relatively lower where $k_{\mathrm{pll}P} = 0.45$ rad/Vs, $k_{\mathrm{pll}I} = 8$ rad/Vs^2. Through the figure, it can be seen that under the condition of low PLL bandwidth, the increase of L_g can suppress the low frequency oscillation. Especially when $L_g = 1.2$ mH, the system is completely stable and the oscillation has disappeared, which agrees with the theoretical analysis of Part C in Section IV. However, due to the limitation of the output power and the grid inductor shown in (25), the maximum L_g is 1.54 mH when the output power is 150 kW. Therefore, when L_g is greater than 1.54 mH, the system cannot be stable. As shown in the figure, the system is unstable when $L_g = 2.2$ mH. On the other hand, it can be found that the glitches of the observed frequency of PLL are more and more serious with the increase of L_g. Hence, the high-frequency stability is challenged.

In Fig. 20(b), the gain of the PLL controller is increased to 5 times where $k_{\mathrm{pll}P} = 2.25$ rad/Vs, $k_{\mathrm{pll}I} = 40$ rad/Vs^2. First, it can be seen that the output frequency of PLL is distorted seri-

ously and the amplitude of the glitches are increased obviously. These mean that the high-frequency stable margin is further decreased. But the low-frequency oscillation can still be weakened with the proper increase of grid inductor L_g like $L_g = 0.7$ mH shown in the figure. These phenomena can sufficiently illustrate the different influence of grid inductor L_g on the system low-frequency and high-frequency stability. However, in this situation, the *LCL*-Filtered single-stage PV generator is dominated by the high-frequency stability and its maximum acceptable ability for the grid inductor L_g is decreased. Hence, the system becomes unstable when L_g becomes 1.2 mH as shown in the figure, which also agrees with the theoretical analysis of Part C in Section IV.

In conclusion, through Fig. 20, it can be found that the grid inductor L_g has different influence on the low-frequency and high-frequency stability of the *LCL*-Filtered single-stage PV generator. With the increase of L_g, the low-frequency oscillation can be suppressed but the high-frequency stability is challenged. However, through decreasing the PLL bandwidth, this contradiction can be alleviated and the *LCL*-Filtered single-stage PV generator is easier to adapt the weak grid.

VI. Conclusion

In this paper, a stability analysis method based on the DF method is proposed to analyze the power oscillation issues of the *LCL*-Filtered single-stage PV generator when it is connected to the weak grid. Being different from the conventional analysis method, the complete model of the *LCL*-Filtered single-stage PV generator is taken into consideration in the proposed analysis method including dc voltage control and nonlinear discontinuous P&O based power control, which effectively enhances the accuracy and completeness of the results. Especially for the critically stable state, both the oscillation amplitude and frequency can be calculated accurately based on the DF method. At the same time, different influence factors are analyzed quantitatively and it is found that the operation points, grid strength and the interaction of multiple control loops influence the system stability greatly. Furthermore, it is first revealed that the grid inductor has different influence on the system high-frequency and low-frequency stability, and this contradiction can be alleviated through decreasing the PLL bandwidth. Finally, the HIL tests are conducted and the results can verify the theoretical analyses well.

References

[1] M. Fortunato, A. Giustiniani, G. Petrone, G. Spagnuolo, and M. Vitelli, "Maximum power point tracking in a one-cycle-controlled single-stage photovoltaic inverter," *IEEE Trans. Ind. Electron.*, vol. 55, no. 7, pp. 2684–2693, Jul. 2008.

[2] F. A. S. Neves, M. Carrasco, F. Mancilla-David, G. M. S. Azevedo, and V. S. Santos, "Unbalanced grid fault ride-through control for single-stage photovoltaic inverters," *IEEE Trans. Power Electron.*, vol. 31, no. 4, pp. 3338–3347, Apr. 2016.

[3] W. Libo, Z. Zhengming, and L. Jianzheng, "A single-stage three-phase grid-connected photovoltaic system with modified MPPT method and reactive power compensation," *IEEE Trans. Energy Convers.*, vol. 22, no. 4, pp. 881–886, Dec. 2007.

[4] L. A. Serpa, S. Ponnaluri, P. M. Barbosa, and J. W. Kolar, "A modified direct power control strategy allowing the connection of three-phase inverters to the grid through LCL filters," *IEEE Trans. Ind. Appl.*, vol. 43, no. 5, pp. 1388–1400, Sep. 2007.

[5] K. Jalili and S. Bernet, "Design of *LCL* filters of active-front-end two-level voltage-source converters," *IEEE Trans. Ind. Electron.*, vol. 56, no. 5, pp. 1674–1689, May 2009.

[6] H. Liu, X. Xie, and W. Liu, "An oscillatory stability criterion based on the unified dq-frame impedance network model for power systems with high-penetration renewables," *IEEE Trans. Power Syst.*, vol. 33, no. 3, pp. 3472–3485, May 2018.

[7] R. Shah, N. Mithulananthan, and K. Y. Lee, "Large-Scale PV plant with a robust controller considering power oscillation damping," *IEEE Trans. Energy Convers.*, vol. 28, no. 1, pp. 106–116, Mar. 2013.

[8] N. Rashidirad, M. Hamzeh, K. Sheshyekani, and E. Afjei, "High-Frequency oscillations and their leading causes in DC microgrids," *IEEE Trans. Energy Convers.*, vol. 32, no. 4, pp. 1479–1491, Dec. 2017.

[9] D. Pan, X. Ruan, C. Bao, W. Li, and X. Wang, "Capacitor-Current-Feedback active damping with reduced computation delay for improving robustness of LCL-type grid-connected inverter," *IEEE Trans. Power Electron.*, vol. 29, no. 7, pp. 3414–3427, Jul. 2014.

[10] D. Yang, X. Ruan, and H. Wu, "Impedance shaping of the grid-connected inverter with LCL filter to improve its adaptability to the weak grid condition," *IEEE Trans. Power Electron.*, vol. 29, no. 11, pp. 5795–5805, Nov. 2014.

[11] M. Lu, A. Al-Durra, S. M. Muyeen, S. Leng, P. C. Loh, and F. Blaabjerg, "Benchmarking of stability and robustness against grid impedance variation for LCL-Filtered grid-interfacing inverters," *IEEE Trans. Power Electron.*, vol. 33, no. 10, pp. 9033–9046, Oct. 2018.

[12] J. Xu, S. Xie, B. Zhang, and Q. Qian, "Robust grid current control with impedance-phase shaping for LCL-Filtered inverters in weak and distorted grid," *IEEE Trans. Power Electron.*, vol. 33, no. 12, pp. 10240–10250, Dec. 2018.

[13] X. Zhou *et al.*, "Robust grid-current-feedback resonance suppression method for LCL-type grid-connected inverter connected to weak grid," *IEEE J. Emerg. Sel. Topics Power Electron.*, vol. 6, no. 4, pp. 2126–2137, Dec. 2018.

[14] J. Sun, "Impedance-based stability criterion for grid-connected inverters," *IEEE Trans. Power Electron.*, vol. 26, no. 11, pp. 3075–3078, Nov. 2011.

[15] X. Chen, Y. Zhang, S. Wang, J. Chen, and C. Gong, "Impedance-Phased dynamic control method for grid-connected inverters in a weak grid," *IEEE Trans. Power Electron.*, vol. 32, no. 1, pp. 274–283, Jan. 2017.

[16] S. Sang, N. Gao, X. Cai, and R. Li, "A novel power-voltage control strategy for the grid-tied inverter to raise the rated power injection level in a weak grid," *IEEE J. Emerg. Sel. Topics Power Electron.*, vol. 6, no. 1, pp. 219–232, Mar. 2018.

[17] S. Zhou *et al.*, "An improved design of current controller for LCL-Type grid-connected converter to reduce negative effect of PLL in weak grid," *IEEE J. Emerg. Sel. Topics Power Electron.*, vol. 6, no. 2, pp. 648–663, Jun. 2018.

[18] A. D. Paquette and D. M. Divan, "Virtual impedance current limiting for inverters in microgrids with synchronous generators," *IEEE Trans. Ind. Appl.*, vol. 51, no. 2, pp. 1630–1638, Mar. 2015.

[19] H. Xin, L. Huang, L. Zhang, Z. Wang, and J. Hu, "Synchronous instability mechanism of P-f droop-controlled voltage source converter caused by current saturation," *IEEE Trans. Power Syst.*, vol. 31, no. 6, pp. 5206–5207, Nov. 2016.

[20] L. Huang, H. Xin, Z. Wang, L. Zhang, K. Wu, and J. Hu, "Transient stability analysis and control design of droop-controlled voltage source converters considering current limitation," *IEEE Trans. Smart Grid*, to be published, doi: 10.1109/TSG.2017.2749259.

[21] S. Zhu *et al.*, "Global asymptotic stability assessment of three-phase inverters with saturation," *IET Power Electron.*, vol. 11, no. 9, pp. 1556–1565, Jul. 2018.

[22] T. Hu, "A nonlinear-system approach to analysis and design of power-electronic converters with saturation and bilinear terms," *IEEE Trans. Power Electron.*, vol. 26, no. 2, pp. 399–410, Feb. 2011.

[23] D. Engels, "The describing functions for a constrained-range integration process with bang-bang input and dead zone," *IEEE Trans. Autom. Control*, vol. 12, no. 5, pp. 582–585, Oct. 1967.

[24] H. Li, S. Wang, J. Lü, X. You, and X. Yu, "Stability analysis of the shunt regulator with nonlinear controller in PCU based on describing function method," *IEEE Trans. Ind. Electron.*, vol. 64, no. 3, pp. 2044–2053, Mar. 2017.

[25] A. Sangwongwanich, Y. Yang, and F. Blaabjerg, "High-Performance constant power generation in grid-connected PV systems," *IEEE Trans. Power Electron.*, vol. 31, no. 3, pp. 1822–1825, Mar. 2016.
[26] H. D. Tafti, A. I. Maswood, G. Konstantinou, J. Pou, and F. Blaabjerg, "A general constant power generation algorithm for photovoltaic systems," *IEEE Trans. Power Electron.*, vol. 33, no. 5, pp. 4088–4101, May 2018.
[27] B. Wen, D. Boroyevich, R. Burgos, P. Mattavelli, and Z. Shen, "Analysis of D-Q small-signal impedance of grid-tied inverters," *IEEE Trans. Power Electron.*, vol. 31, no. 1, pp. 675–687, Jan. 2016.
[28] M. G. Villalva, J. R. Gazoli, and E. R. Filho, "Comprehensive approach to modeling and simulation of photovoltaic arrays," *IEEE Trans. Power Electron.*, vol. 24, no. 5, pp. 1198–1208, May 2009.

Yanghong Xia (S'16) was born in Hubei Province, China. He received the B.S. degree in automation from the College of Automation, Huazhong University of Science and Technology, Wuhan, China, in 2014. He is currently working toward the Ph.D. degree with the College of Electrical Engineering, Zhejiang University, Hangzhou, China.

His current research interests include nonlinear control, distributed generations, and microgrids.

Miao Yu (M'16) received the B.S. degree in automation in 2007 from the College of Electrical Engineering, Zhejiang University, Hangzhou, China, where he received the Ph.D. degree in control science and engineering in 2012.

From 2013 to 2015, he was with Aalto University, Helsinki, Finland, as a Postdoctoral Researcher. Since 2016, he has been working with the College of Electrical Engineering, Zhejiang University, as an Associate Professor. He has authored or coauthored more than 20 technical papers in journal and conferences. His current research interests include control strategies in microgrid and renewable power generation.

Xiaoming Wang was born in Yunnan Province, China, in 1993. He received the B.S. degree in automation from the College of Electrical Engineering, Zhejiang University, Hangzhou, China, in 2011. He is currently working toward the Ph.D. degree with the College of Electrical Engineering, Zhejiang University, Hangzhou.

His current research interests include modeling, control, and stability of distributed power systems.

Wei Wei received the B.Eng. degree in automation, the M.Eng. degree in control theory and control engineering, and the D.Eng. degree in power electronics and electronic drives all from the College of Electrical Engineering, Zhejiang University, Hangzhou, China, in 1983, 1986, and 1994, respectively.

He is currently a Professor with the College of Electrical Engineering, Zhejiang University. His currently research interests includes intelligent control, the development of novel technology of renewable energy and smart grids.